Engineering Fracture Mechanics 226 (2020) 106887

Contents lists available at ScienceDirect

Engineering Fracture Mechanics

journal homepage: www.elsevier.com/locate/engfracmech

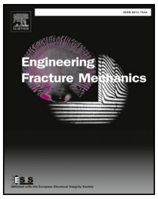

High-cycle fatigue and fracture behavior of double-side friction stir welded 6082Al ultra-thick plates

C. Yang[a,b], B.B. Wang[a], B.H. Yu[a], L.H. Wu[a], P. Xue[a,*], X.M. Zhang[c], G.Z. He[c], D.R. Ni[a,*], B.L. Xiao[a], K.S. Wang[d], Z.Y. Ma[a]

[a] *Shenyang National Laboratory for Materials Science, Institute of Metal Research, Chinese Academy of Sciences, 72 Wenhua Road, Shenyang 110016, China*

[b] *School of Materials Science and Engineering, University of Science and Technology of China, 72 Wenhua Road, Shenyang 110016, China*

[c] *CRRC Changchun Railway Vehicles Co., Ltd., Changchun 130062, China*

[d] *School of Metallurgical Engineering, Xi'an University of Architecture and Technology, Xi'an 710055, China*

ARTICLE INFO

Keywords:
Ultra-thick aluminum alloy plate
Double-side friction stir welding
High-cycle fatigue
Microstructure, mechanical properties
Residual stress

ABSTRACT

For welded structures of precipitation-strengthened aluminum alloys, achieving sound joint with good fatigue property is not an easy task, especially for thick plates. In the present work, ultra-thick 6082Al-T4 alloy plates with 80 mm in thickness were double-side friction stir welded and heat-treated. The high cycle fatigue (HCF) property and fracture behavior of the joint were investigated using trisection specimens in thickness, and the key factors that affect the fracture behavior were addressed. High quality joint was achieved with the three-layered specimens fractured along the lowest hardness zone (LHZ) in the static tensile testing. Further, the fatigue life curves exhibited almost the same distribution tendency, and the same fatigue limit (110 MPa) and fatigue ratio (0.49) were achieved in the three-layered specimens. During fatigue testing, the middle and lower layers fractured along the LHZ, which was similar to those during the static tensile tests, while abnormal fracture occurred in the nugget zone (NZ) of the upper specimen. Further examination revealed that the residual stress in the NZ of the upper layer was tensile stress (+9 MPa) whereas it was compressive stress in the lower layer (–31 MPa). The tensile residual stress together with the external loaded cyclic tensile stress resulted in more serious fatigue damage in the upper layer and led to the abnormal fracture in the NZ.

1. Introduction

Welding and joining are essential methods for structural components, whereas fusion welding processes are extremely challenging for Al alloy plates and the issue can become significantly serious when thick Al alloy plates are involved [1–3]. Friction stir welding (FSW), as an effective solid state joining technique, has over years achieved prominent progress in joining light alloys [4–6], composites [7,8] and dissimilar materials [9,10]. FSW can avoid the disadvantages encountered in fusion welding of Al alloys [4,5]. It is widely reported that joints with excellent properties of thin and medium thick alloy plates could be achieved by acquiring specific microstructures produced with process variants based on one-side FSW [11–14]. Therefore, it is highly expected to apply FSW

Abbreviations: FSW, friction stir welding; NZ, nugget zone; TMAZ, thermo-mechanically affected zone; HAZ, heat-affected zone; BM, base material; LHZ, lowest hardness zone; UTS, ultimate tensile strength; HCF, high cycle fatigue

[*] Corresponding authors.

E-mail addresses: pxue@imr.ac.cn (P. Xue), drni@imr.ac.cn (D.R. Ni).

https://doi.org/10.1016/j.engfracmech.2020.106887
Received 14 November 2019; Received in revised form 6 January 2020; Accepted 13 January 2020

to weld thick Al alloy plates based on its excellent advantages in the welding of thin Al alloy plates.

Fatigue property, as a significant evaluation index, is of great importance to estimate the reliability of welded structure components. FSW joints are usually expected to have superior fatigue properties to fusion welds by acquiring fine recrystallized grains in the nugget zone with a high fraction of high angle grain boundaries [15–17]. However, FSW joint is an inhomogeneous structure, and its fatigue properties are affected by complex factors. It is well documented that the fatigue property of metal is dominated by the interaction of grain size, precipitates, dislocation configuration, substructures and also residual stress [18–21]. The dominant factors can therefore be classified as the following two: microstructure and residual stress. It's hence crucial to make the two affecting factors clear thoroughly.

The residual stress is inevitable in welding structures due to the intensive hot deformation. Although the residual stress in FSW joints can be decreased to a great extent compared to that by fusion welding [7,21,22], it cannot be underestimated in many situations, especially for the thick plates. The residual stress together with the external loaded cyclic stress may greatly affect the fatigue crack initiation and propagating rate [22–25]. Usually, the tensile residual stress can accelerate the crack propagation whereas the compressive residual stress can retard the crack propagation [24–26]. However, this issue will become more complicated when ultra-thick Al alloy joints are involved, because the inhomogeneity will be more inclined to generate through the thickness direction.

Systematic studies evaluating the fatigue properties of thin and medium thick Al alloy FSW joints have been widely reported [14,27–31] and the fracture mechanisms have also been declared. However, there are few related researches involved ultra-thick Al alloy plates. Some investigations at present focused on the plates that were less than 45 mm in thickness without the evaluation of the fatigue properties [32–36]. Although an ultra-thick SiC_p/2014Al composite plate with 120 mm in thickness [3] and a 108 mm thick 5A06 Al alloy plate [37] were reported to be welded successfully with FSW respectively, fatigue properties were not addressed and welding defects were easily formed in the FSW joints of ultra-thick plates. Moreover, the limited research on the fatigue properties of Al alloy thick plates was investigated on the hot-rolled Al-Cu-Li alloy plate with a thickness of 90 mm [38], rather than the FSW joint. It's therefore essential to demonstrate the fatigue properties in the FSW joints of ultra-thick Al alloy plates. In the present work, we mainly focused on the high cycle fatigue (HCF) properties of the FSW joints of 6082Al ultra-thick plates, intending to explore the dominant factors that affect the fatigue fracture behavior.

2. Experiment

In the present work, as-extruded 6082Al-T4 alloy plates were used as the base material (BM) with dimensions of 2000 mm × 800 mm × 80 mm. The chemical composition of the BM is as follows: 0.90 Mg, 0.89 Si, 0.017 Zn, 0.045 Cu, 0.19 Fe, 0.6Mn, 0.042 Cr, 0.021 Ti, and balance Al (wt.%).

Double-side butt welding was carried out on a FSW machine (JM50 × 40-1) with the welding direction parallel to the extruding direction of the BM. The double-side welds were completed in sequence and the second pass welding was conducted after the first pass on the other side of the plates. The welding was conducted at a tool rotation rate of 400 rpm and a welding speed of 100 mm/min. A welding tool with a shoulder diameter of 55 mm and a truncated cone pin with right-hand thread and three flats was used. The diameter of the pin was 20 mm at the root and 6 mm at the tip, and the length of the pin was 45 mm. Post-weld heat-treatment with a temperature of 175 °C for 7 h, was performed on the as-welded plates subsequently.

Microstructural observations were conducted using optical microscopy (OM, Axiovert 200 MAT), with the samples machined perpendicular to the welding direction and polished, then etched in a 2.5 vol% HNO_3, 1.5 vol% HCl, 1.0 vol% HF and 95 vol% H_2O mixed acid reagent. Electron backscattered diffraction (EBSD, HKL Channel 5 System) was conducted to reveal the grain structures, with the samples electro-polished in a reagent ($HClO_4$: C_2H_5OH = 1:9, vol.%) for 1 min at − 25 °C and 12 V. The precipitation evolution was observed using transmission electron microscopy (TEM, FEI TECNAI F20). Samples for TEM observation were prepared by twin-jet electro-polishing with a solution of 30% HNO_3 and 70% CH_3OH at –30 °C and 15 V.

Vickers hardness values were measured on the cross-section of the welds perpendicular to the welding direction. The tests were conducted using an automatic machine (Leco, LM-247AT) under a load of 300 g holding for 15 s. Fourteen lines with 41 indentations in each line were measured to acquire the hardness distribution maps with a total of 574 indentations. The interval between lines was 4 mm and 1.5 mm between indentations. Three lines of the indentations were selected to examine the hardness profiles of the upper layered specimen before and after the fatigue testing using the same parameters above.

The FSW joints were sliced into three pieces along the thickness direction for the tensile tests, i.e., the lower layer (the first-pass weld layer), the middle layer (including overlapped region), and the upper layer (the second-pass weld layer). The specimens were machined perpendicular to the FSW direction with a gauge scale of 80 mm × 22 mm × 21 mm. The specimens were electrical discharge machined and ground with SiC papers up to grit #800 to achieve a smooth surface. An SANS CMT 5205 testing machine was used to conduct the tensile test at room temperature with an initial strain rate of $1 \times 10^{-3}\ s^{-1}$ and a testing speed of 4.8 mm/min. Three specimens for each layer were conducted to acquire an average value.

High-cycle fatigue tests were conducted using a hydraulic servo fatigue testing system (Instron 8850). The specimens were prepared with the same size as those for the tensile tests and were milled and polished to achieve a smooth surface. Sine waveform with a stress ratio of R = 0.1 was applied at a frequency of 30 Hz. After the fatigue testing, the crack initiation sites and propagation path were examined using scanning electron microscopy (SEM, ZEISS SUPRA 55). The schematic diagrams of the position and the size of the specimens are presented in Fig. 1.

Residual stress measurement was conducted on a KJS-3P type stress testing instrument with a BE120-05AA-A type strain gage. A sectioning relaxation strain-gage method according to GB/T 31218-2014 was selected in the testing. The specimens used for fatigue

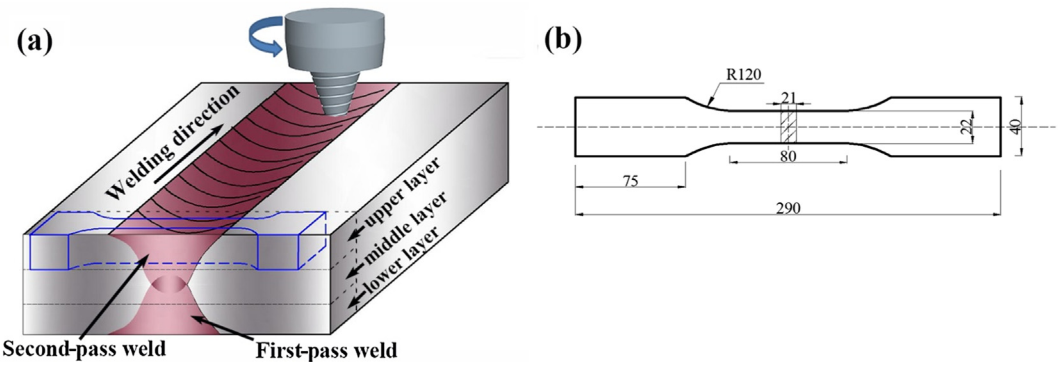

Fig. 1. Schematic diagrams of (a) sampling position, (b) tensile and fatigue specimens.

testing were chosen to conduct the residual stress measurement, as shown in Fig. 1b. The strain gage was set in the center of specific zones to be tested and then a slice on the surface of the specimen in a dimension of 15 × 12 × 1 mm^3 was sectioned to detect the strain relaxation. Eight dots were measured in the centers of the NZs and HAZs on the surfaces of both the upper and lower specimens. The determination of the residual stress by sectioning the relaxation strain-gage method in specific zones is schematically listed in Fig. 2.

3. Results and discussion

3.1. Microstructures

Fig. 3 shows the cross-sectional macrostructure and the EBSD maps of specific regions in the NZ of the joint. The double-side welding process produced a dumbbell-shaped weld, consisting of two single-pass welds, as seen from Fig. 3f. In our previous investigation [39], the microstructures of the joint have been discussed in detail. The onion ring structure and “S” line in the NZ had no devastating effects on the mechanical properties. It is well known that the material in NZ of a FSW joint experiences intense plastic deformation, which may induce the different dynamic recrystallization (DRX) and grain morphology in different regions, especially for the FSW joint of ultra-thick plate [11,40,41]. Fig. 3a–e show the grain structures of the regions A ~ E in the NZ marked with yellow dotted line rectangles in Fig. 3f. The black lines represented the high angle grain boundaries (HAGBs, ≥15°), whereas the red lines indicated the low angle grain boundaries (LAGBs, < 15°) in the images. As can be seen, there is an obvious grain size gradient in the NZ through the thickness direction. Regions A and E (i.e. the top regions of each single-pass weld NZ) had almost the same grain size while the smallest grain size appeared in region C (overlapped region of the two-pass NZs) with a high fraction of LAGBs.

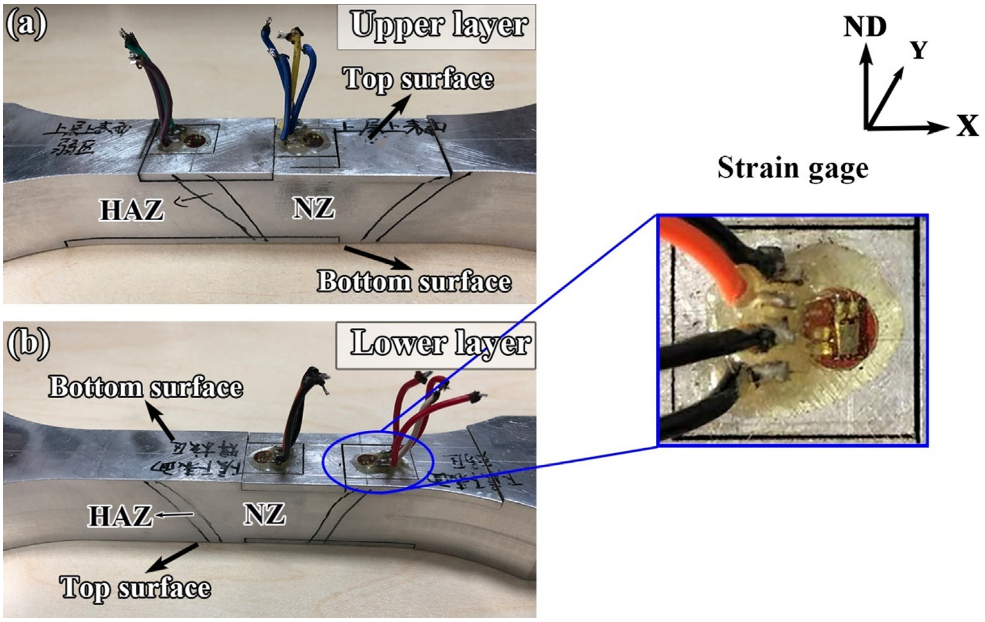

Fig. 2. Stress determination by sectioning relaxation strain-gage method for: (a) upper layer, (b) lower layer.

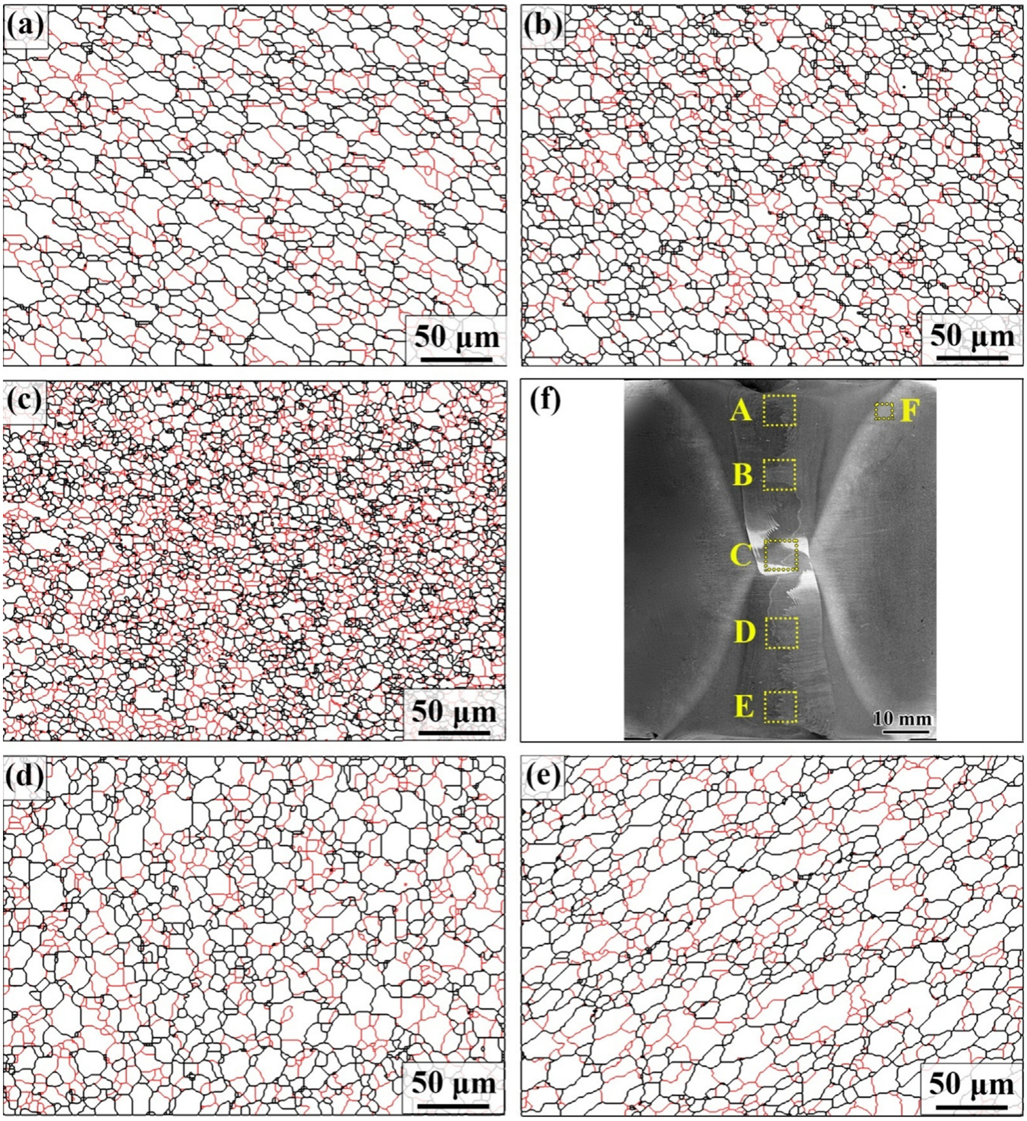

Fig. 3. EBSD maps of different regions in the NZ: (a) region A, (b) region B, (c) region C, (d) region D and (e) region E, (f) cross-sectional macrostructure of joint.

Fig. 4 shows the bright-field TEM images of the NZ and HAZ in the upper weld corresponding to the yellow rectangles A and F in Fig. 3f. The incident direction of the electron beam was parallel to the ⟨1 0 0⟩ zone axis of the Al matrix. As can be seen that the NZ was characterized by needle-shaped precipitates (β''), which were main strengthening precipitates under the peak aging condition for 6000 series Al alloys [42,43]. While in the HAZ, it was characterized by coarsened precipitates with some needle-shaped ones retained.

In the last work, we have discussed the precipitates evolution after the double-side FSW in detail and previous studies have also clearly clarified the precipitation sequence for 6000 series Al alloys during aging [39,42–45]. In the NZ, the precipitates experienced intense plastic deformation and thermal cycles that led to complex microstructure evolution including dissolution, precipitation and redissolution [42], and finally appeared as β'' phase after the FSW and post-weld aging (Fig. 4a). The precipitates in HAZ only underwent the thermal cycles that led to partly coarsening with some fine needle-shaped ones retained after the FSW and post-weld aging (Fig. 4b).

3.2. Microhardness and tensile properties

The hardness value distribution of the whole weld, as discussed in the previous study [39], exhibited a “butterfly” type and presented a symmetrical distribution with the center line. The values in the top and bottom areas in the NZ were of the same level as the BM. The lowest hardness zone (LHZ) was located in the HAZ, which presented a “hyperbola” shaped distribution. The

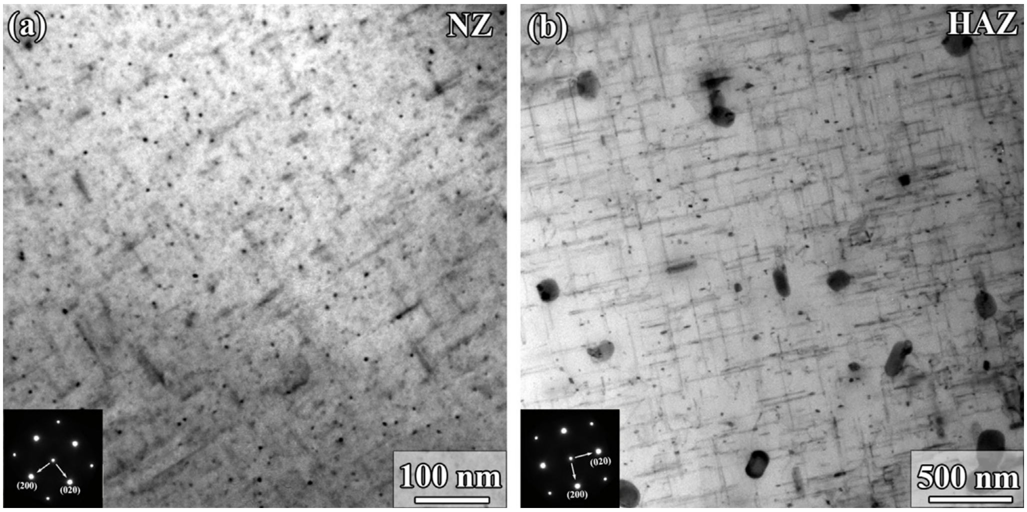

Fig. 4. Bright-field TEM images of characteristic zones in the upper layer of joint: (a) NZ, (b) HAZ.

precipitation behavior during welding and subsequent post-weld aging contributed strongly to the hardness recovery in the top area of each single-pass NZ, which contained a high density of β'' phase (Fig. 4a). On the contrary, the low hardness values in the HAZ were induced by the coarsened precipitates (Fig. 4b).

The UTS values of the layered specimens were listed in Table 1. A prediction of the UTS for the whole joint could be made from the tensile results of the layered specimens [46]. The fracture path of the tensile specimen was along the LHZ, which has a good match with the microhardness distribution. Severe local deformation occurred in one side randomly in HAZ at advancing side (AS) or retreating side (RS) with obvious necking, which can be seen in Fig. 5a.

3.3. Fatigue properties and fracture behavior

The relationship between the fatigue life and the maximum stresses (*S-N* curves) for the BM and the layered specimens of the FSW joint are presented on log-log scale, as shown in Fig. 6. The *S-N* curves showed that the fatigue life of different layers exhibited nearly the same distribution tendency where the same fatigue limits ($\sigma_{0.1}$, 110 MPa) and fatigue ratios (ratio of $\sigma_{0.1}/\sigma_b$, 0.49) were obtained in all the three-layered specimens.

According to the well-established Basquin law [47–49], the stress controlled fatigue life is closely linked to the stress amplitudes that can be expressed as following:

$$\sigma_a = \sigma_f^{'}(2N_f)^b \tag{1}$$

where, $\sigma_f{}'$ is the fatigue strength coefficient, and b is called the fatigue strength exponent or Basquin exponent. The values of $\sigma_f{}'$and b are closely associated with the intrinsic material microstructures and properties and they directly dominate the fatigue life at certain stress amplitudes [48,49]. Fitting results of $\sigma_f{}'$and b according to Fig. 6 were listed in Table 1. Although the $\sigma_f{}'$ of the lower layer was a little higher than the other two layers, the b value was decreased slightly, leading to the same fatigue limits. For the three layers, the similar UTS and grain morphology led to the same fatigue limits, which meant that two-pass welding did not induce an intrinsic difference of the HCF properties for different layers.

Fig. 5b and c show the typical macrographs of the failure locations of the layered specimens after fatigue testing. A phenomenon can be observed that the upper layered specimens fractured in the NZ at typical low and high maximum stresses, which was different from the other two layers. The fracture behaviors of the other two-layered specimens had a good match with the static tensile results where the specimens fractured in the traditional weak zones, i.e., the HAZs.

It is well known that the FSW joint is a non-uniform structure including four different zones with different microstructure and properties, i.e., the BM, HAZ, TMAZ and NZ. For the common FSW joints of precipitation-strengthened thin and medium thick Al

Table 1
Tensile strength and HCF property results of BM and layered specimens.

Sample ID	UTS, MPa	$\sigma_{0.1}$, MPa	Fatigue ratio	$\sigma_f{}'$, MPa	b
BM	320	180	0.56	410	−0.052
Upper layer	230	110	0.49	676	−0.113
Middle layer	225	110	0.49	728	−0.117
Lower layer	223	110	0.49	756	−0.120

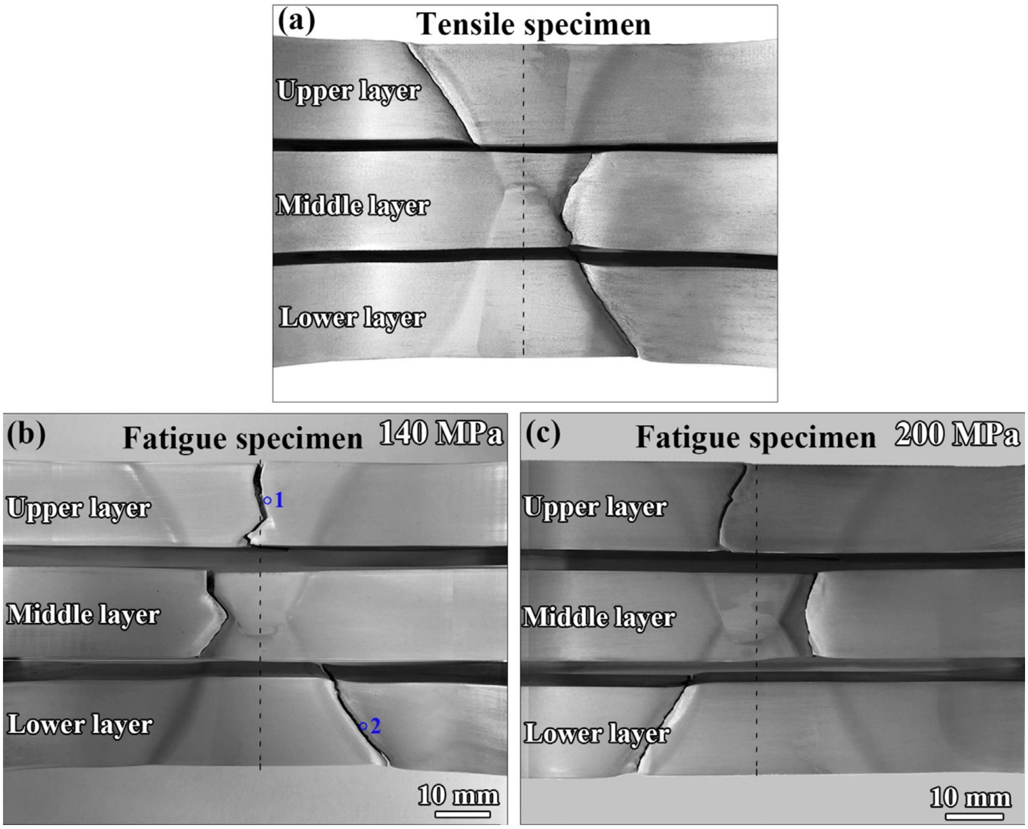

Fig. 5. Typical macrograph of failed locations of (a) static tensile specimens, (b) layered specimens at maximum stress of 140 MPa, (c) layered specimens at maximum stress of 200 MPa.

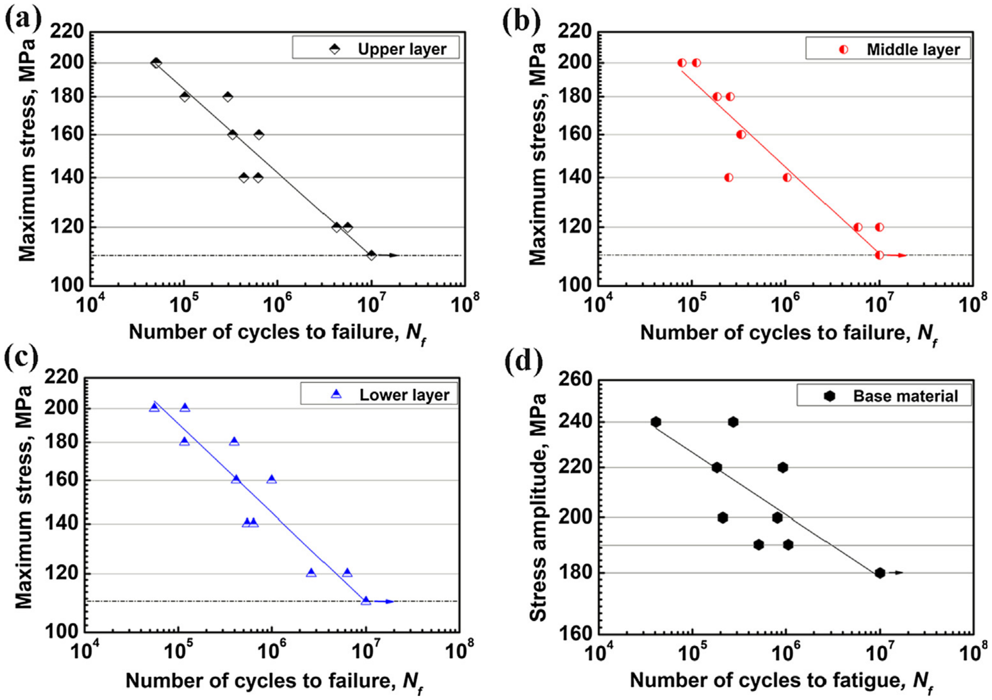

Fig. 6. *S-N* curves of: (a) upper layer, (b) middle layer, (c) lower layer and (d) BM.

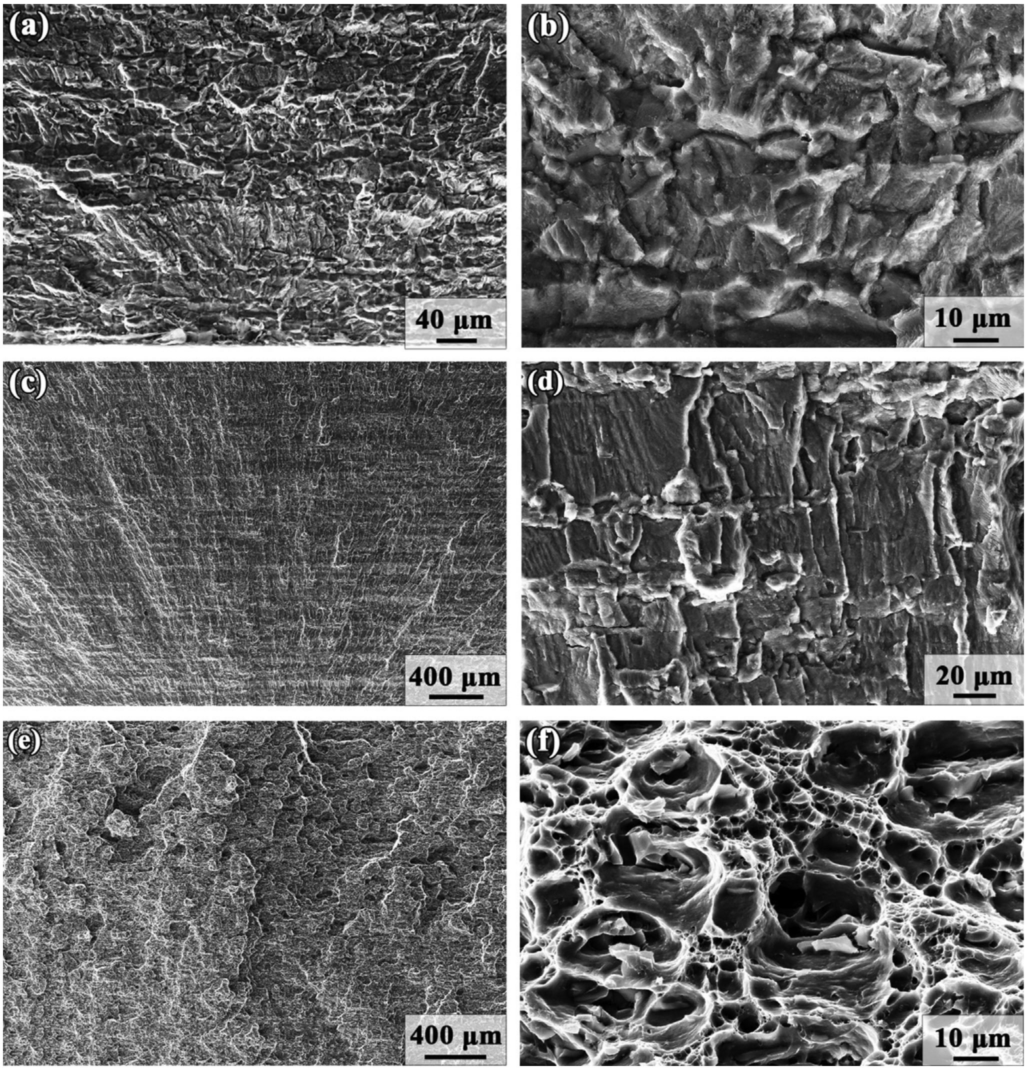

Fig. 7. Fractographs of different sub-zones of the upper layered specimen failed at the maximum stress of 140 MPa: (a), (b) crack initiation zone; (c), (d) crack propagating zone; (e), (f) fast fracture zone.

alloy plates, the specimens always failed in the softened HAZ during the fatigue testing under the cyclic stress loading [49]. While for the FSW joints of thick Al alloy plates, an inhomogeneity existed through the thickness direction besides the various zones across the joint, which will result in a more complicated situation [50]. It has been discussed that the fatigue damage of metal material was dominated by various factors: grain size, precipitates, dislocation configuration, substructures and residual stress [18–21]. As a result, these influencing factors will also exhibit an inhomogeneous distribution through the thickness direction. The abnormal fracture will definitely be dominated by one or the interaction of several factors.

To investigate the abnormal fracture mechanism of the upper layer, the microstructure evolution near the fracture position was further analyzed. Fig. 7 shows the typical fractographs of the upper layer that fractured in the NZ under a low maximum stress of 140 MPa. Three characteristic zones, i.e. crack initiation zone (Fig. 7a and b), crack propagating zone ((Fig. 7c and d)) and fast fracture zone (Fig. 7e and f) were obviously observed. It can be seen that the crack initiated from the specimen surface, and the free surfaces of the specimens were usually documented to be the prior initiation positions for Al alloys [18,22]. After crack initiating, the crack began to propagate till failure, and the crack propagating zone presented a fan-shaped pattern and no obvious fatigue striations and second crack were observed. The fast fracture zone was characterized by dimples showing ductile fracture morphology in this zone.

The TEM images near the fracture positions of the upper and lower layered specimens at the maximum stress of 140 MPa were presented in Fig. 8. The corresponding sampling positions were marked in Fig. 5b with blue circles. The cyclic loading during the fatigue deformation exerted on the specimens would induce the dislocation emission and motion, and the interaction of dislocations or the interaction of dislocations and precipitates would further facilitate the crack initiating [48–50]. Based on the microstructures near the fracture positions in both the upper and lower layered specimens, no obvious dislocation configurations were observed. The

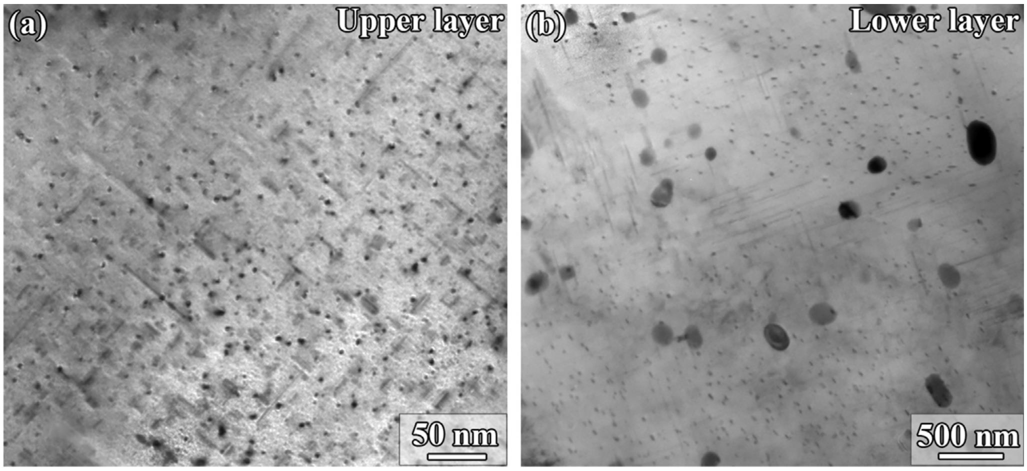

Fig. 8. Bright field TEM images near the fracture positions of the layered specimens at the maximum stress of 140 MPa: (a) upper layer fractured in NZ, (b) lower layer fractured in HAZ.

upper layered specimen fractured in the NZ, which was characterized by fine-needle shaped precipitates (Fig. 8a). The lower layered specimen fractured in HAZ that was characterized by many coarsened precipitates (Fig. 8b). Despite the coarsening of the precipitates in HAZ that would induce weakening, the fracture still occurred in the NZ for the upper layered specimen. Therefore, the precipitation evolution was not the dominant factor for the abnormal fracture of the upper layered specimens.

Fig. 9 shows the hardness curves on the cross-section of the upper layered specimen before and after the fatigue testing. The initial hardness profile exhibited a typical “W” shape which is similar to that of the one-side FSW joint of thin Al alloy plate [23,45,46]. It was obviously observed that the hardness values in the NZ and LHZ were kept almost the same as that of the untested specimen, which proved that no hardening effect occurred in the HAZ during fatigue tests. The phenomenon further confirmed that microstructural evolution did not affect the abnormal fracture phenomenon.

To further confirm the dominant factor of the abnormal fracture phenomenon, the residual stress was examined on the surfaces of both the upper and lower layered specimens. The testing sites were selected in the centers of the NZ and HAZ on the top and bottom surfaces of the specimens. The testing results of biaxial residual stresses were listed in Table 2 (X axis:perpendicular to the welding direction; Y axis:along welding direction). The stress values were acquired according to the following equation [48,49]:

$$\begin{cases} \sigma_x = \frac{E}{1-\nu^2}(\varepsilon_x + \nu\cdot\varepsilon_y) \\ \sigma_y = \frac{E}{1-\nu^2}(\varepsilon_y + \nu\cdot\varepsilon_x) \end{cases} \tag{2}$$

There have been systematic studies associating with the residual stress distribution of the one-side FSW joints of thin and medium thick Al alloy plates [7,21,24,51]. The distribution trend of the residual stress in one-side FSW Al alloy joints was well documented to have an typical “M” shape with tensile residual stress in the NZ and HAZ and the peak values appeared in the HAZ [21,52–54]. Limited reports demonstrated the distribution of the residual stress in the FSW joints of thick Al alloy plates, and its effect on fatigue behavior is not clear. Canaday et al. [35] studied the residual stress distribution through the thickness of the FSW joint of 32 mm thick 7050Al alloy plates, which presented an “M” shaped distribution, as reported in thin Al alloy plates, with the tensile residual stress decreasing from the top to the bottom of the NZ. Moreover, the residual stresses of a dissimilar FSW joint of 7050Al and 2024Al

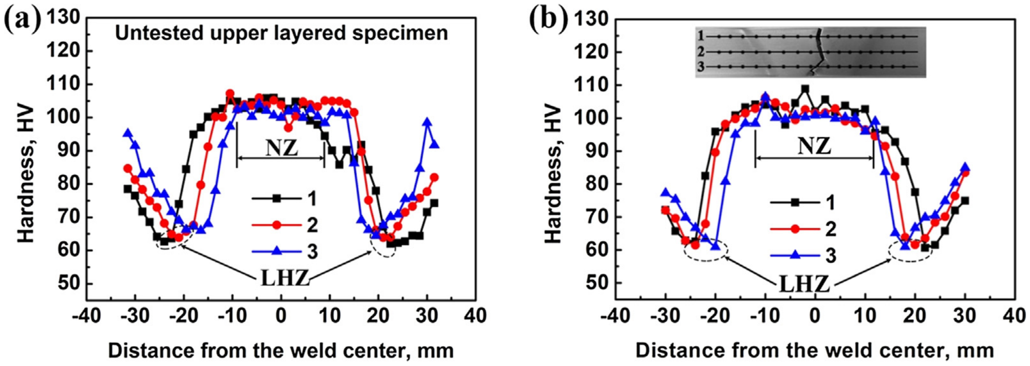

Fig. 9. Hardness curves of the upper layered specimen: (a) untested specimen, (b) specimen after fatigue testing at a maximum stress of 140 MPa.

Table 2
Residual stress values of the upper and lower layered specimens (negative values indicate compressive residual stress, positive values represent tensile residual stress).

Position		Residual stress value, MPa	
		X axis direction	Y axis direction
Upper layer	Top-surface NZ	9	–13
	Bottom surface NZ	1	0
	Top-surface HAZ	–30	–27
	Bottom-surface HAZ	–4	2
Lower layer	Top-surface NZ	–31	–13
	Bottom surface NZ	–29	–2
	Top-surface HAZ	–27	–12
	Bottom-surface HAZ	–26	–34

plates 25.4 mm in thickness was measured by Prime et al. [33] using neutron diffraction and synchrotron X-ray diffraction, and the results also showed an “M” shape through the thickness with tensile residual stress in NZ and HAZ. From these two studies, it is indicated that the existence of residual might affect the fatigue behavior of the FSW joints, but no experimental evidences were provided.

In the present work, the situations were not the same for both the lower and upper layered specimens. It can be seen that the NZ and HAZ of the lower layered specimen showed compressive residual stresses along the X axis direction. However, for the upper layered specimen, the tensile residual stress appeared in the center of the NZ and it was compressive residual stress in the HAZ along the X axis direction.

The maximum residual stress as high as 20–70% of the yield strength can generate along the welding direction of the FSW Al alloy joints [7,21,22,33]. However, in the present work, the residual stress (–13 MPa) in the center of NZ on the top surface was ~5% of the yield strength for the upper layered specimen and it was ~17% for the lower layer along the welding direction (Y axis direction), which were much lower than that of the reported level. Ma et al. [52] investigated the effect of the specimen size on the residual stress distribution, showing that the peak value of the residual stress decreased obviously with the decreasing of specimen size. Therefore, the specimen size plays a significant role in affecting the residual stress values because the cutting and machining processes would induce the relaxation of the residual stress [55].

Obviously, the different states of the residual stresses between the upper and lower layered specimens dominated the abnormal fracture phenomenon. The existed tensile residual stress in the NZ together with the external applied cyclic tensile loading would facilitate the initiation of the micro-crack [56] and the crack propagated subsequently till fractured in the NZ for the upper layered specimen. On the contrary, the compressive residual will hinder the crack formation to certain extent [14,21,24–26], so the crack still initiated from the HAZ for the lower layered specimen. As a result, the difference of the residual stress distribution led to the abnormal fracture in the NZ of the upper layered specimen.

4. Conclusion

In the present work, ultra-thick 6082Al alloy plates were successfully welded using double-side FSW method, and the HCF property and fracture behavior of the FSW joints were investigated in detail. The conclusions are as follows:

1. Though microstructural inhomogeneity existed through the thickness direction, almost same UTS were achieved for the layered specimens and the tensile failure positions had a good agreement with the hardness distribution.
2. The distribution of the fatigue life for the three layers presented nearly the same tendency with a same fatigue limit of 110 MPa and same fatigue ratio of 0.49.
3. The middle and lower layered specimens failed in the HAZ during fatigue tests, which were corresponding to the static tensile failure locations. However, the upper layered specimen exhibited an abnormal fracture in the NZ.
4. The abnormal fracture was proved to be induced by the duplicate effect of the tensile residual stress in the NZ and the applied cyclic tensile loading for the upper layered specimen.

Declaration of Competing Interest

The authors declare that they have no known competing financial interests or personal relationships that could have appeared to influence the work reported in this paper.

Acknowledgments

This work was supported by the Youth Innovation Promotion Association of the Chinese Academy of Sciences (2017236) and National Natural Science Foundation of China under grant No. U1760201.

Appendix A. Supplementary material

Supplementary data to this article can be found online at https://doi.org/10.1016/j.engfracmech.2020.106887.

References

[1] Zhang ZH, Dong SY, Wang YJ, Xu BS, Fang JX, He P. Microstructure characteristics of thick aluminum alloy plate joints welded by fiber laser. Mater Des 2015;84:173–7.

[2] Rathod DW, Sun Y, Obasi G, Roy MJ. Effect of multiple passes on Lüders/yield plateaus, microstructure and tensile behaviour of narrow-gap thick-section weld plates. J Mater Sci 2019;54:12833–50.

[3] Qiao Q, Su Y, Ouyang Q, Zhang D, Song X, Guo LJ. Microstructural characterization and mechanical properties of 120-mm ultra-thick SiCp/Al composite plates joined by double-sided friction stir welding. Metall Mater Trans A 2019;50:3589–602.

[4] Mishra RS, Ma ZY. Friction stir welding and processing. Mater Sci Engng, R 2005:1–78.

[5] Padhy GK, Wu CS, Gao S. Friction stir based welding and processing technologies-processes, parameters, microstructures and applications: a review. J Mater Sci Technol 2018;34:1–38.

[6] Wang W, Han P, Peng P, Zhang T, Liu Q, Yuan SN, et al. Friction stir processing of magnesium alloys: a review. Acta Metall Sin (Engl Lett), doi:10.1007/s40195-019-00971-7.

[7] Zhang XX, Ni DR, Xiao BL, Andrä H, Gan WM, Hofmann M, et al. Determination of macroscopic and microscopic residual stresses in friction stir welded metal matrix composites via neutron diffraction. Acta Mater 2015;87:161–73.

[8] Wang C, Wang BB, Wang D, Xue P, Wang QZ, Xiao BL, et al. High-speed friction stir welding of SiCp/Al-Mg-Si-Cu composite. Acta Metall Sin (Engl Lett) 2019;32:677–83.

[9] Wu LH, Nagatsuka K, Nakata K. Direct joining of oxygen-free copper and carbon-fiber-reinforced plastic by friction lap joining. J Mater Sci Technol 2018;34:192–7.

[10] Xue P, Xiao BL, Ni DR, Ma ZY. Enhanced mechanical properties of friction stir welded dissimilar Al-Cu joint by intermetallic compounds. Mater Sci Engng, A 2010;527:5723–7.

[11] Wu LH, Hu XB, Zhang XX, Li YZ, Ma ZY, Ma XL, et al. Fabrication of high-quality Ti joint with ultrafine grains using submerged friction stirring technology and its microstructural evolution mechanism. Acta Mater 2019;166:371–85.

[12] Zeng XH, Xue P, Wu LH, Ni DR, Xiao BL, Wang KS, et al. Microstructural evolution of aluminum alloy during friction stir welding under different tool rotation rates and cooling conditions. J Mater Sci Technol 2019;35:972–81.

[13] Xue P, Wang BB, An XH, Ni DR, Xiao BL, Ma ZY. Improved cyclic softening behavior of ultrafine-grained Cu with high microstructural stability. Scr Mater 2019;166:10–4.

[14] Wang BB, Xue P, Xiao BL, Wang WG, Liu YD, Ma ZY. Achieving equal fatigue strength to base material in a friction stir welded 5083-H19 aluminium alloy joint. Sci Tech Weld Join 2020;25:81–8.

[15] Ericsson M, Sandstrom R. Influence of welding speed on the fatigue of friction stir welds, and comparison with MIG and TIG. Int J Fatigue 2003;25:1379–87.

[16] Moreira PMGP, De Figueiredo MAV, De Castro PMST. Fatigue behavior of FSW and MIG weldments for two aluminum alloys. Theor Appl Fract Mech 2007;48:169–77.

[17] Texier D, Atmani F, Bocher P, Nadeau F, Chen J, Zedan Y, et al. Fatigue performance of FSW and GMAW aluminum alloys welded joints: competition between microstructural and structural-contact-fretting crack initiation. Int J Fatigue 2018;116:220–33.

[18] Biro AL, Chenelle BF, Lados DA. Processing, microstructure, and residual stress effects on strength and fatigue crack growth properties in friction stir welding: a review. Metall Mater Trans B 2012;43:1622–37.

[19] Wicke M, Brueckner-Foit A, Kirsten T, Zimmermann M, Buelbuel F, Christ HJ. Near-threshold crack extension mechanisms in an aluminum alloy studied by SEM and X-ray tomography. Int J Fatigue 2019;119:102–11.

[20] Altamura A, Straub D. Reliability assessment of high cycle fatigue under variable amplitude loading: Review and solutions. Engng Fract Mech 2014;122:40–66.

[21] Ni DR, Chen DL, Xiao BL, Wang D, Ma ZY. Residual stresses and high cycle fatigue properties of friction stir welded SiCp/AA2009 composites. Int J Fatigue 2013;55:64–73.

[22] Zhang XX, Wu LH, Andrä H, Gan WM, Hofmann M, Wang D, et al. Effects of welding speed on the multiscale residual stresses in friction stir welded metal matrix composites. J Mater Sci Technol 2019;35:824–32.

[23] Li XT, Jiang XY. Theoretical analyses of nano-crack nucleation near the main crack tip in nano and micro crystalline materials. Engng Fract Mech 2019;221(106672):1–15.

[24] Aliha MRM, Gharehbaghi H. The effect of combined mechanical load/welding residual stress on mixed mode fracture parameter of a thin aluminum cracked cylinder. Engng Fract Mech 2017;180:213–28.

[25] Shen F, Zhao B, Li L, Chua CK, Zhou K. Fatigue damage evolution and lifetime prediction of welded joints with the consideration of residual stresses and porosity. Int J Fatigue 2017;103:272–9.

[26] Semari Z, Aid A, Benhamena A, Amrouche A, Benguediab, Sadok A, Benseddiq N. Effect of residual stresses induced by cold expansion on the crack growth in 6082 aluminum alloy. Engng Fract Mech 2013;99:159–68.

[27] Miranda ACO, Gerlich A. Walbridge. Aluminum friction stir welds: review of fatigue parameter data and probabilistic fracture mechanics analysis. Engng Fract Mech 2015;147:243–60.

[28] Ma YE, Xia ZC, Jiang RR, Li WY. Effect of welding parameters on mechanical and fatigue properties of friction stir welded 2198–T8 aluminum-lithium alloy joints. Engng Fract Mech 2013;114:1–11.

[29] Li MJ, Shi YJ, Pan QL, Zhang Y, Lu GX, Guan SK, Birbilis N. Low anisotropy of fatigue crack growth in Al-5.8Mg-0.25Sc. Int J Fatigue 2019;125:170–8.

[30] Li M, Goyal A, Doquet V, Ranc N, Couzinié JP. Ultrafine versus coarse grained Al 5083 alloys: From low-cycle to very-high cycle fatigue. Int J Fatigue 2019;121:84–97.

[31] Vysotskiy I, Malopheyev S, Rahimi S, Mironov S, Kaibyshev R. Unusual fatigue behavior of friction-stir welded Al–Mg–Si alloy. Mater Sci Engng, A 2019;760:277–86.

[32] Mao YQ, Ke LM, Liu FC, Chen YH, Xing L. Investigations on temperature distribution, microstructure evolution, and property variations along thickness in friction stir welded joints for thick AA7075-T6 plates. Int J Adv Manuf Technol 2016;86:141–54.

[33] Prime MB, Herold TG, Baumann JA, Lederich RJ, Bowden DM, Sebring RJ. Residual stress measurements in a thick, dissimilar aluminum alloy friction stir weld. Acta Mater 2006;54:4013–21.

[34] Rao TS, Rao SRK, Reddy GM. Friction stir welding of thick section Al-Zn-Mg-Cu aluminum alloy. Materialwiss Werkstofftech 2018;49:851–8.

[35] Canaday CT, Moore MA, Tang W, Renolds AP. Through thickness property variations in a thick plate AA7050 friction stir welded joint. Mater Sci Engng, A 2013;559:678–82.

[36] Liang ZM, Wang X, Cai CW, Wang DL. Microstructure and mechanical properties of thick plate friction stir welds for 6082–T6 aluminum alloy. High Temp Mater Proc 2019;38:525–32.

[37] Guo N, Fu YL, Wang YZ, Meng Q, Zhu YX. Microstructure and mechanical properties in friction stir welded 5A06 aluminum alloy thick plate. Mater Des 2017;113:273–83.

[38] Wu PF, Deng YL, Zhang J, Fan ST, Zhang XM. The effect of inhomogeneous microstructures on strength and fatigue properties of an Al-Cu-Li thick plate. Mater Sci Engng, A 2018;731:1–11.

[39] Yang C, Zhang JF, Ma GN, Wu LH, Zhang XM, He GZ, et al. Microstructure and mechanical properties of double-side friction stir welded 6082Al ultra-thick plates. J Mater Sci Technol 2020;41:105–16.

[40] Prangnell PB, Heason CP. Grain structure formation during friction stir welding observed by the stop action technique. Acta Mater 2005;53:3179–92.

[41] Deng XM, Xu SM. A study of texture patterns in friction stir welds. Acta Mater 2008;56:1326–41.

[42] Sato YS, Kokawa H, Enomoto M, Jogan S. Microstructural evolution of 6063 aluminum during friction stir welding. Metall Mater Trans A 1999;30:2429–37.

[43] Sato YS, Kokawa H, Enomoto M, Jogan S, Hashimato T. Precipitation sequence in friction stir weld of 6063 aluminum during aging. Metall Mater Trans A 1999;30:3125–30.

[44] Maruyama N, Uemori R, Hashimoto N, Saga M, Kikuchi M. Scr Mater 1997;36:89–93.

[45] Liu FC, Ma ZY. Influence of tool dimension and welding parameters on microstructure and mechanical properties of friction stir welded 6061–T651 aluminum alloy. Metall Mater Trans A 2008;39:2378–88.

[46] Xu WF, Luo YX, Zhang W, Fu MW. Comparative study on local and global mechanical properties of bobbin tool and conventional friction stir welded 7085–T7452 aluminum thick plate. J Mater Sci Technol 2018;34:173–84.

[47] Zhang ZF, Liu R, Zhang ZJ, Tian YZ, Zhang P. Exploration on the unified model for fatigue properties prediction of metallic materials. Acta Metall Sin 2018;54:1694–704.

[48] An XH, Lin QY, Wu SD, Zhang HF. Improved fatigue strengths of nanocrystalline Cu and Cu-Al alloys. Mater Res Lett 2015;3:135–41.

[49] Basquin OH. The exponential law of endurance tests. Am Soc Test Mater 1910;10:625–30.

[50] Jian HG, Luo J, Tang XM, Li X, Yan C. Influence of microstructure on fatigue crack propagation behaviors of an aluminum alloy: Role of sheet thickness. Engng Fract Mech 2017;180:105–14.

[51] James MN, Hughes DJ, Hattingh DG, Bradley GR, Mills G, Webster PJ. Synchrotron diffraction measurement of residual stresses in friction stir welded 5383–H321 aluminium butt joints and their modification by fatigue cycling. Fatigue Fract Engng Mater Struct 2004;27:187–202.

[52] Ma YE, Staton P, Fischer T, Irving PE. Size effects on residual stress and fatigue crack growth in friction stir welded 2195–T8 aluminium-Part I: Experiments. Int J Fatigue 2011;33:1417–25.

[53] Xu WF, Liu JH, Zhu HQ. Analysis of residual stresses in thick aluminum friction stir welded butt joints. Mater Des 2001;32:2000–5.

[54] Peel M, Steuwer A, Preuss M, Withers PJ. Microstructure, mechanical properties and residual stresses as a function of welding speed in aluminium AA5083 friction stir welds. Acta Mater 2003;51:4791–801.

[55] Jones KW, Bush RW. Investigation of residual stress relaxation in cold expanded holes by the slitting method. Engng Fract Mech 2017;179:213–24.

[56] Indriyantho BR, Zreid I, Kaliske M. Finite strain extension of a gradient enhanced microplane damage model for concrete at static and dynamic loading. Engng Fract Mech 2019;216(106501):1–24.